The Longwave Cloud-radiative Feedback in Tropical Waves Derived by Different Precipitation Datasets

Wei-Ting Hsiao[1], **Eric D. Maloney**[1]

[1]Department of Atmospheric Science, Colorado State University, Fort Collins, CO, USA

Key Points:

- GPCPv3.2 has less frequent precipitation between 10-40 mm day^{-1}, but more frequent precipitation at other intensities than in GPCPv1.3
- The radiative feedback calculated by GPCPv3.2 is weaker than in GPCPv1.3 over most of the spatiotemporal spectral domain
- Radiation anomalies lag precipitation in eastward-propagating Kelvin and mixed Rossby-gravity waves in GPCPv3.2, but not in GPCPv1.3

Corresponding author: Wei-Ting Hsiao, `WeiTing.Hsiao@colostate.edu`

Abstract

The tropical longwave cloud-radiative feedback is calculated using outgoing longwave radiation (OLR) and precipitation in two versions of Global Precipitation Climatology Project, version 1.3 (GPCPv1.3) and the newer version 3.2 (GPCPv3.2). GPCPv3.2 has less frequent precipitation between 10-40 mm day^{-1} but more frequent precipitation at other intensities than in GPCPv1.3. The radiative feedback on intraseasonal timescales calculated by GPCPv3.2 is weaker than in GPCPv1.3 by almost half. The radiative feedbacks are also found to have a red-noise like distribution in spatiotemporal spectral space in both precipitation products, but the magnitudes are weaker in GPCPv3.2. OLR lags precipitation by phase angles of up to 40° in eastward-propagating Kelvin and n = 0 inertia-gravity waves in GPCPv3.2, but not in GPCPv1.3. The updated magnitudes and phase shift of the feedback may modify our understanding of tropical disturbances such as the Madden-Julian oscillation.

Plain Language Summary

High-altitude, widespread anvil clouds are generated when heavy convective precipitation occurs in the tropics. These clouds are not only a passive product produced by convection, but they also can subsequently enhance convection by trapping upward infrared radiative flux emitted by the Earth, effectively heating the atmosphere. This additional radiative heating effect can induce upward motion in the tropics, supporting the convective systems by transporting more humid air from below. However, the strength of this cloud-radiative feedback is hard to estimate because global, continuous observations of surface precipitation are difficult to derive. In this study, the strength of the radiative feedback is calculated using the same product of observed radiative heating against two different observational precipitation products. The more recent improved precipitation product yields much weaker radiative feedback strengths for all types of tropical weather systems. In addition, cloud-radiative heating is found to substantially lag behind precipitation in certain fast, eastward-propagating tropical rainfall systems in the newer precipitation observational product, unlike the older one. Why such a lag exists is unclear. The discrepancy of the estimation of cloud-radiative feedback strengths and properties in the older versus the newer precipitation products indicates that our understanding of mechanisms supporting tropical disturbances is still incomplete.

1 Introduction

Tropical disturbances affect global extreme weather and the hydrological cycles through their moist dynamics and associated teleconnections (e.g., Ferrett et al., 2020; Frank & Roundy, 2006; Maloney & Hartmann, 2000; Tseng et al., 2018). Convective systems and cloudiness are commonly coupled with tropical equatorial waves (Takayabu, 1994; Wheeler & Kiladis, 1999), and the longwave cloud-radiative feedback generated by convective anvil clouds serves as an important mechanism modifying the development of these waves. In the Madden-Julian oscillation (MJO), the presence of convective anvil clouds traps more longwave radiation in precipitating regions, imposing a heating effect on the atmosphere (Del Genio & Chen, 2015; Johnson et al., 2015; Johnson & Ciesielski, 2000; Lin & Mapes, 2004; Ma & Kuang, 2011). The radiative heating enhances upward velocity near the precipitation maximum, consistent with weak horizontal temperature gradient theory, which helps moisten the atmosphere and destabilize the MJO (Adames & Kim, 2016; Andersen & Kuang, 2012; Benedict et al., 2020; Chikira, 2014; Crueger & Stevens, 2015; Hu & Randall, 1994; M.-I. Lee et al., 2001; Raymond, 2001; A. Sobel et al., 2014; A. Sobel & Maloney, 2012; Wolding & Maloney, 2015; Zurovac-Jevtić et al., 2006). Longwave cloud-radiative feedbacks have also been suggested to support tropical cyclones (Ruppert et al., 2020), and to damp equatorial Kelvin waves but support equatorial Rossby waves (Andersen & Kuang, 2012; Benedict et al., 2020; Medeiros et al., 2021).

Longwave cloud-radiative feedbacks can be described and measured in a variety of ways. In simple models relevant to the moisture mode theory for disturbances such as the MJO, the feedback is represented using a "greenhouse enhancement factor", such that anomalous radiative heating is proportional to precipitation multiplied by a constant factor (Raymond, 2001; A. H. Sobel & Gildor, 2003; A. Sobel & Maloney, 2012; Sugiyama, 2009). The factor aims to roughly describe how much radiative heating coexists with a fixed amount of latent heat released by the phase change of water in the atmospheric column. Prior studies have shown that the radiative feedback parameter is dependent on zonal wavelength in observed datasets (Adames & Kim, 2016) and precipitation magnitude in general circulation models (Kim et al., 2015). The feedback has been incorporated into the "effective" gross moist stability parameter that effectively reducing the efficiency of moist static energy discharge from the column in regions of convection (e.g., Bretherton & Sobel, 2002; Raymond et al., 2009; Su & David Neelin, 2002). Estimating the greenhouse enhancement factor is the main focus of this paper.

Knowing accurate magnitudes of cloud-radiative feedbacks is important for validating the known theories of tropical disturbances and helps improve weather and climate predictions (e.g., Dias et al., 2021; Hsiao, Hwang, et al., 2022; Hsiao, Barnes, et al., 2022; M.-I. Lee et al., 2001; Medeiros et al., 2021). For example, the moisture mode theory of the MJO heavily relies on the presence of radiative feedbacks to help maintain the moisture field that supports MJO convection (e.g., Adames & Kim, 2016; Jiang et al., 2020; A. Sobel & Maloney, 2012; Zhang et al., 2020), and how the radiative feedback is represented in weather and climate models can affect predictions not only in the tropics, but also in other regions through teleconnections. Nevertheless, estimating the longwave cloud-radiative feedback using observations is difficult. To estimate the feedback, accurate observations of outgoing longwave radiation (OLR) are needed, which is possible through passive remote sensing by spaceborne satellites (Doelling et al., 2016; H.-T. Lee et al., 2007; Liebmann & Smith, 1996). In contrast, obtaining accurate global, continuous observations of surface precipitation are challenging due to scarce in-situ observations and large uncertainties in satellite retrievals (e.g., Bolvin et al., 2021; Prakash et al., 2013; Prakash & Gairola, 2014; Prigent, 2010). In this paper, we examine the sensitivity of the longwave cloud-radiative feedback using two versions of Global Precipitation Climatology Project (GPCP) products and the same OLR dataset.

2 Methodology

2.1 Data

Global daily precipitation products, GPCP version 1.3 (GPCPv1.3; also known as GPCP 1DD; Huffman et al., 2001) and version 3.2 (GPCPv3.2; also known as GPCP-DAY; Huffman et al., 2023), are used. The main update for GPCPv3.2 is to replace the Threshold Matched Precipitation Index (TMPI) with the Integrated Multi-satellite Retrievals for GPM (IMERG) product, associated with inclusion of spaceborne precipitation radar observations from the Tropical Rainfall Measuring Mission (TRMM; Kummerow et al., 1998) and the Global Precipitation Mission (GPM; Hou et al., 2014). GPCPv3.2 has been shown to outperform GPCPv1.3 in oceanic regions in measures of frequency of occurrence of different rain rates (Li et al., 2023).

Negative anomalies of National Oceanic and Atmospheric Administration Interpolated OLR (NOAA OLR; Liebmann & Smith, 1996) are used as a proxy for anomalous atmospheric column-integrated radiative heating. This allows direct comparison to results of previous studies (e.g., Adames & Kim, 2016; Lin & Mapes, 2004). Two other OLR products that include satellite observations independent from those used by NOAA OLR, the NOAA Climate Data Record (CDR) of Daily OLR Version 1.2 (H.-T. Lee et al., 2007), and Clouds and the Earth's Radiant Energy System (CERES) synoptic 1-degree (SYN1deg) Edition 4.1 observed daily OLR (Doelling et al., 2016), are also used to test

the sensitivity of results to the OLR product used (Figures S1-S3 in the Supplemental Material).

All datasets used have a grid spacing of 1° (latitude) × 1° (longitude), except GPCPv3.2 with 0.5° × 0.5° grid spacing. All data is regridded conservatively onto the 1° × 1° grid of NOAA OLR. The study uses data from 1 September 2000 to 31 August 2021 to obtain results unless otherwise noted.

2.2 Signal filtering

In section 3.2, a 20-100 day Lanczos band-pass filter with a 101-day window is applied onto precipitation and radiative heating rates to isolate signals relevant to the MJO, with further refinements by planetary zonal wavenumber (k). The associated greenhouse enhancement factor is then calculated as the negative of the slope of linearly regressing OLR onto precipitation anomalies. The 95% confidence intervals (CI) derived using the Student t-test are calculated involving procedures in Bretherton et al. (1999), as described in Text S1 in the Supplemental Material.

The relationship between OLR and precipitation in other parts of wavenumber-frequency (k–ω) space is also examined. Following Wheeler and Kiladis (1999), we calculate the wave-form OLR amplitude (R), precipitation amplitude (P), and the phase shift between wave-form OLR and precipitation (φ_R) in $k-\omega$ space using the following procedure. OLR and precipitation for the whole time span are detrended and the first three harmonics of the annual cycle are removed to obtain anomalies. Spatiotemporal Fourier decomposition is applied to the anomalies following Hayashi (1971) using 128-day windows with 10-day Hanning tapering at both ends, and shifted consecutively by a day for adjacent estimates. The power spectra, co-spectra, and quadrature spectra are calculated at each latitude, averaged in 15°S-15°N, and then averaged over all time. R, P, and φ_R can then be calculated using these averaged quantities. Finally, the radiative feedback parameter in $k-\omega$ space, $r(k,\omega)$, is calculated at the peak of precipitation:

$$r = \frac{R\cos(\varphi_R)}{P} \tag{1}$$

Compared to estimating the feedback parameter by directly dividing R by P in spectral space (e.g., Inoue et al., 2020), a non-zero phase lag would lead to a smaller feedback parameter onto precipitation.

3 Results

3.1 Precipitation and radiative feedback in climatology

General differences between the two GPCP precipitation products are first examined (Figure 1). Figure 1a demonstrates a very different histogram of observed surface precipitation rates in GPCPv1.3 and v3.2 at higher values, with GPCPv3.2 having more counts above 50 mm day^{-1} compared to GPCPv1.3. GPCPv1.3 has no observations above 100 mm day^{-1}. Similar to Figure 1a but isolating lighter precipitation using a logarithmic scale, Figure 1b shows that GPCPv3.2 has more observations of light precipitation ($< 10^{0.6} \approx 4.0$ mm day^{-1}) but has fewer observations of moderate-to-strong precipitation ($> 10^{0.6} \approx 4.0$ mm day^{-1} and $< 10^{1.5} \approx 32$ mm day^{-1}) than GPCPv1.3. GPCPv1.3 also has fewer observations of heavy precipitation ($> 10^{1.5} \approx 32$ mm day^{-1}). These differences are similar to the findings of Li et al. (2023).

A joint histogram of the two GPCP precipitation products is presented in Figure 1c. Consistent with Figure 1a, GPCPv3.2 contains a larger range of precipitation rates from zero to nearly 250 mm day^{-1}, while GPCPv1.3 values mainly span the region from zero to nearly 100 mm day^{-1} (Figure 1c). Focusing on lighter precipitation in Figure 1d,

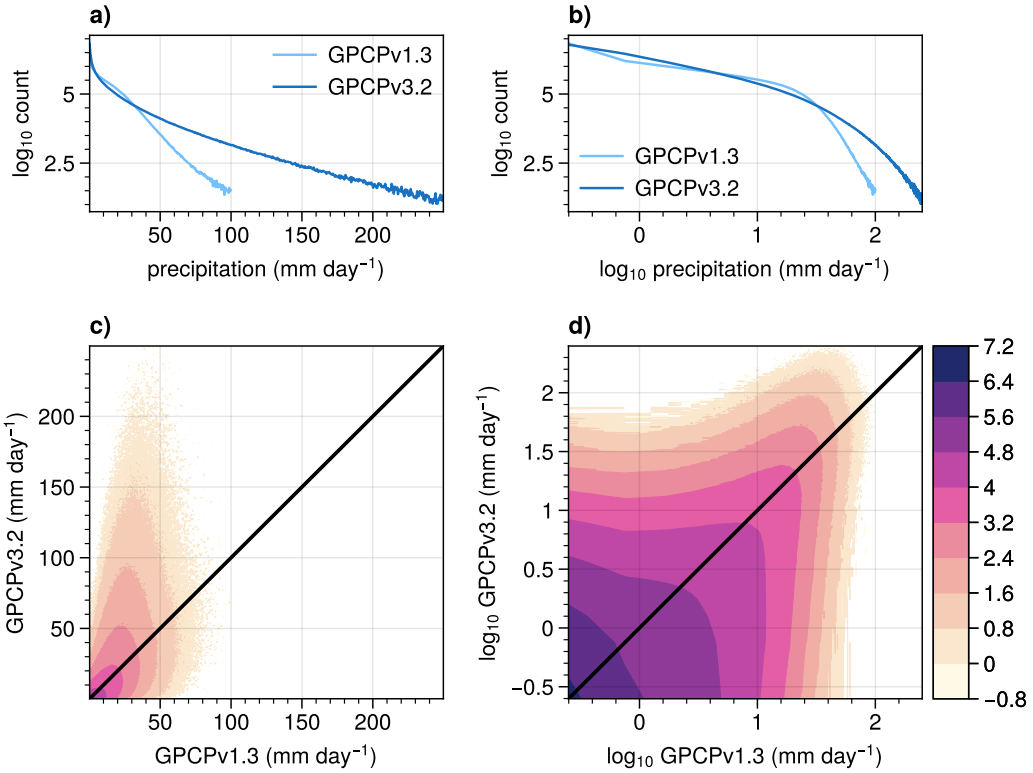

Figure 1. Histograms of precipitation observations in GPCPv1.3 and GPCPv3.2 over the tropics (15°S-15°N) during 1 September 2000 to 31 August 2021, binned every 0.5 mm day^{-1}. (a) shows histograms of each product. (b) as in (a) but uses a logarithmic scale on the precipitation axis. (c) shows a joint histogram of both products, with colors indicating $\log_{10}$ of counts. (d) as in (c) but uses logarithmic scales on both axes. Note that the observation counts are weighted by grid areas and are shown in a logarithmic scale, and the black line in (c-d) is the one-to-one line if the two products produced the same values.

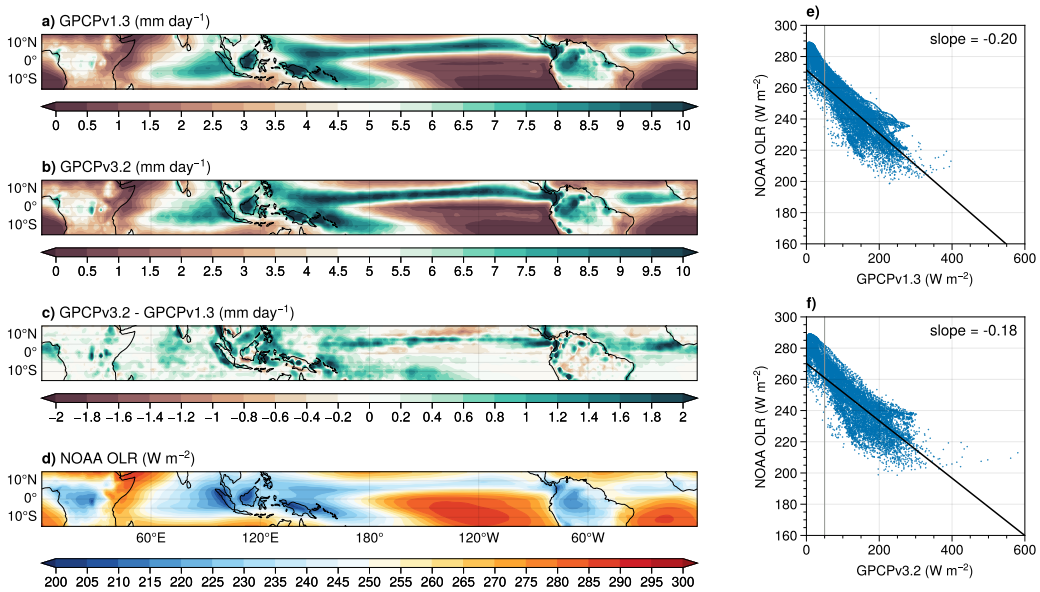

Figure 2. Global annual-mean (a) GPCPv1.3 precipitation, (b) GPCPv3.2 precipitation, (c) the difference between (a) and (b) in mm day^{-1}, and (d) NOAA OLR in W m^{-2}. (e) and (f) show scatter plots between NOAA OLR and GPCPv1.3 and GPCPv3.2 precipitation in units of W m^{-2}, respectively using every grid point. The climatological greenhouse enhancement factor using data above 50 W m^{-2} precipitation rates (vertical gray lines) are annotated at the upper-right corners, and the associated linear-fit lines are shown (black lines).

the histogram contains large counts far from the one-to-one line, indicating that the two precipitation products frequently have very different values. For example, at $10^{0.5} \approx 3.2$ mm day^{-1} in GPCPv1.3, GPCPv3.2 can range from $10^{-0.5} \approx 0.32$ to $10^{0.5} \approx 3.2$ mm day^{-1} with occasional observations up to $10^{1.8} \approx 63.2$ mm day^{-1}.

Figures 2a-c compare the global annual-mean precipitation between the two versions of GPCP precipitation products. While their spatial patterns are qualitatively similar (Figures 2a-b), GPCPv3.2 has generally stronger precipitation where annual-mean precipitation is high, such as in the Indo-Pacific warm pool, the Southern Pacific Convergence Zone (SPCZ), and the Inter-Tropical Convergence Zone (ITCZ), with the ITCZ being narrower in GPCPv3.2 (Figure 2c). To examine the climatological global tropical radiative feedback, the feedback is calculated by comparing the precipitation products to NOAA OLR (Figure 2d) using all grid points following the method used in Peters and Bretherton (2005). Linear regression of OLR to precipitation yields a slightly smaller global feedback parameter in GPCPv3.2, since GPCPv3.2 has higher mean precipitation (Figures 2e-f).

3.2 Precipitation and radiative feedback in tropical waves

Precipitation and its radiative feedback associated with different tropical waves are now examined. The first focus is on the longwave cloud-radiative feedback on intraseasonal timescales, since radiative feedbacks have been suggested to be important to the scale selection and magnitude of the MJO in moisture mode theory (see Introduction). As a direct comparison with Adames and Kim (2016), the greenhouse enhancement factor calculated using 20-100 day filtered anomalies is shown (Figure 3). Without zonal filtering, GPCPv1.3 yields a greenhouse enhancement factor magnitude of 0.15 (Figure

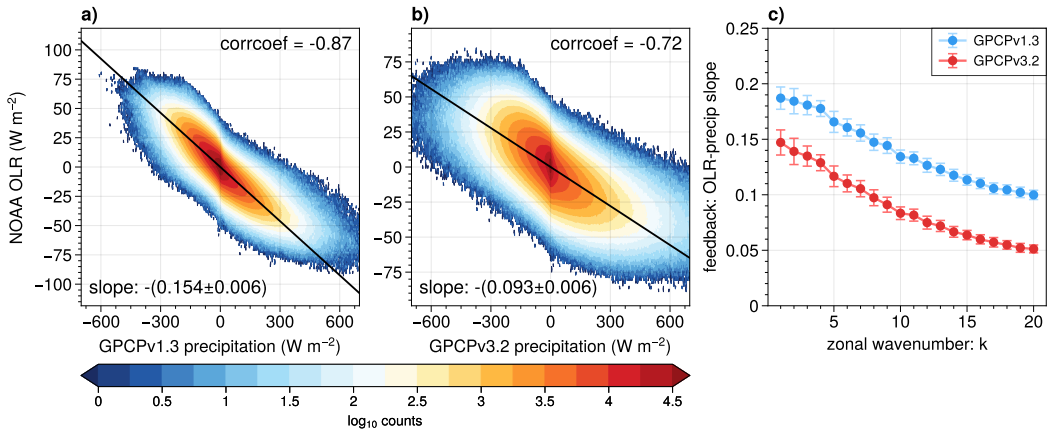

Figure 3. Histograms of 20-100 day filtered OLR and precipitation over the Indo-Pacific warm pool (60°E-180°, 15°S-15°N) using (a) GPCPv1.3 and (b) GPCPv3.2. The contours are $\log_{10}$ counts, and the line shows the best linear prediction of OLR by precipitation, with their slopes (i.e., greenhouse enhancement factor) and their 95% CI and correlation coefficients (corrcoef) annotated. (c) shows the greenhouse enhancement factor calculated using single planetary zonal wavenumbers (k) from each GPCP version, with error bars showing 95% CI.

3a), and GPCPv3.2 yields 0.09 (Figure 3b), close to half of GPCPv1.3. While the two estimations of the greenhouse enhancement factor use the same OLR dataset, Figure 3b has a larger spread on both axes compared to Figure 3a, especially at where precipitation anomalies are positive, consistent with GPCPv3.2 containing heavier precipitation (Figure 1). The larger spread shows that OLR has a less direct correspondence to precipitation in GPCPv3.2, as also shown by its smaller correlation coefficient. It is likely that the abundance of heavy precipitation observed in GPCPv3.2 compared to GPCPv1.3 leads to the smaller slope, or the greenhouse enhancement factor, on 20-100 day timescales. The estimation of the greenhouse enhancement factor is smaller than those proposed in previous studies where it ranged from 0.1-0.2 (Bretherton & Sobel, 2002; Lin & Mapes, 2004; Peters & Bretherton, 2005).

With zonal filtering, GPCPv3.2 also yields weaker feedbacks compared to GPCPv1.3 at all planetary zonal wavenumbers (k; Figure 3c). In the MJO band (k = 1-5), GPCPv1.3 yields greenhouse enhancement factor magnitudes of 0.17-0.19, and GPCPv3.2 yields 0.12-0.15. While the estimated radiative feedbacks from the two products decreases nearly linearly with wavenumbers along a similar slope, how the two provide different preferential growth of waves at lower k is different. For example, the ratio of the greenhouse enhancement factors between those at k = 1 and k = 10 yielded by GPCPv1.3 is 0.19/0.13 = 1.46, while the ratio yielded by GPCPv3.2 is 0.15/0.08 = 1.88. Since the growth rate of the wave linearly increases with the greenhouse enhancement factor in moisture mode theory (Adames & Kim, 2016), GPCPv3.2 implies a faster growth rate of waves with k = 1 relative to k = 10 then in GPCPv1.3. Thus, although the greenhouse enhancement factor is weaker using GPCPv3.2, the scale selection of radiative feedbacks that support the planetary scale of the MJO is stronger in GPCPv3.2.

Next, we examine the longwave cloud-radiative response to precipitation over the entire spectral domain in Wheeler-Kiladis diagrams, as described in subsection 2.2. The power spectrum of precipitation in GPCPv3.2 has larger magnitudes over the whole spectral domain, especially where the power is already large in GPCPv1.3 (Figures 4a-c). The radiative feedback parameter (r) over all planetary wavenumbers and frequencies is also

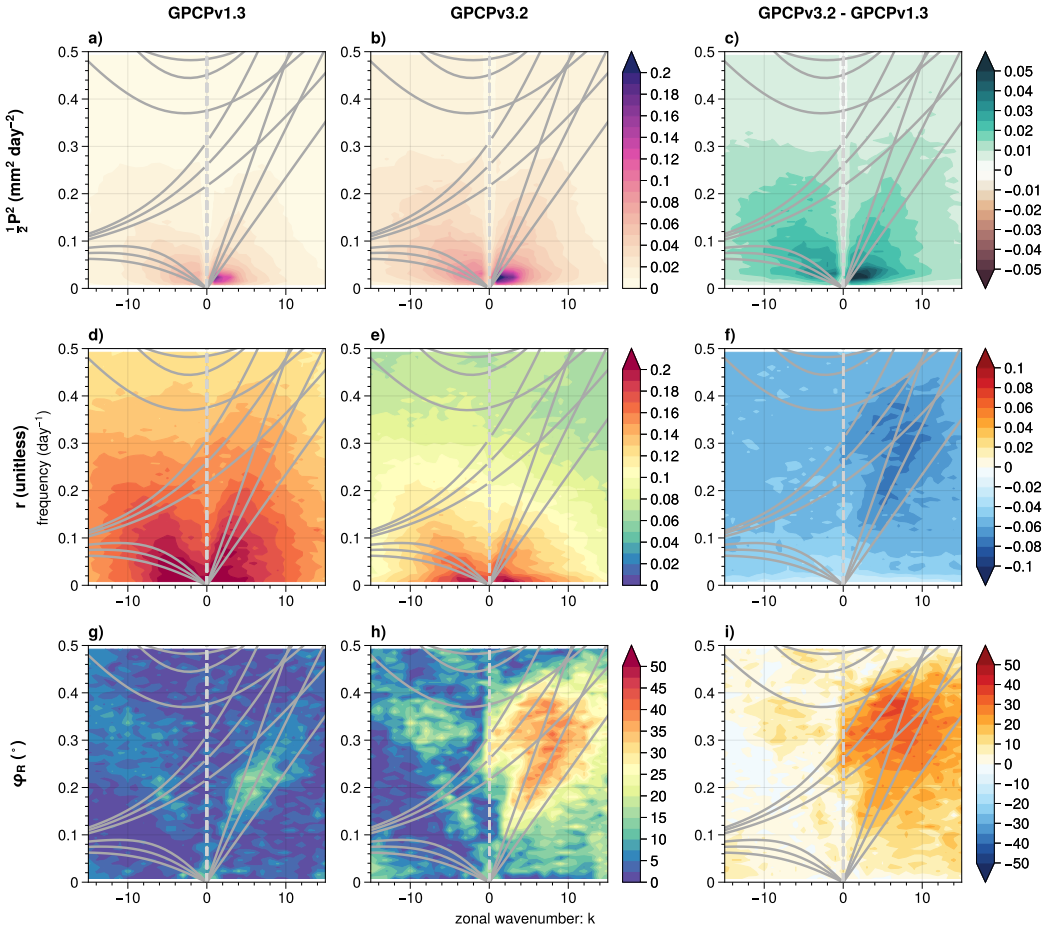

Figure 4. (a) the power spectra of precipitation (mm^2 day^{-2}), (d) the radiative feedback parameter r calculated using the proposed method, and (g) the phase difference between OLR and precipitation (degree). The second column (b,e,h) shows the same quantity as in the first column, but utilizing GPCPv3.2, while the third column (c,f,i) shows their difference (GPCPv3.2 minus GPCPv1.3 results). The gray solid lines are the solutions for convectively coupled equatorial waves at equivalent depths of 12, 25, and 50 m, as shown in Wheeler and Kiladis (1999).

examined following the method proposed in subsection 2.2 (Figures 4d-f). Consistent with Figure 3, r is larger with lower k at low frequencies below 0.1 day^{-1} ($>$ 10-day period). In addition, r generally decreases with increasing frequency, such that the whole feedback spectrum has a red noise-like distribution. Notably, r has local peaks where convectively coupled equatorial waves are active, except for n $\geq$ 1 inertia-gravity waves.

The phase shift between OLR and precipitation (φ_R) shows robust differences between GPCPv3.2 and GPCPv1.3 (Figures 4g-i). Both products yield non-negative φ_R, indicating that OLR anomalies are always in phase with, or lagging, precipitation. In GPCPv1.3, φ_R has a peak of 20° in Kelvin waves at frequencies near 0.2 day^{-1} (5-day period), and a similar but slightly weaker phase shift for its westward-propagating counterpart. However, a very-strong asymmetry between eastward- and westward-propagating waves is shown in φ_R from GPCPv3.2. In the eastward-propagating (k $>$ 0) domain, there are distinct peaks of φ_R of $\sim$40° in n = 0 eastward inertia gravity waves (EIG$_0$) and Kelvin waves, both of which are high-frequency eastward-propagating waves. In the remaining

spectral regions with k > 0, a notable positive difference in φ_R also exists between the two GPCP products, which generates smaller feedback parameter estimations compared to the conventional method that directly divides OLR by precipitation spectral magnitudes (equation 1).

To summarize, larger precipitation variance is found in GPCPv3.2 compared to GPCPv1.3, accompanied by smaller radiative feedback parameter and thus weaker longwave cloud-radiative feedbacks over the whole spectral domain. As a feature much weaker in GPCPv1.3, GPCPv3.2 precipitation robustly leads OLR by nearly 40° in fast eastward-propagating waves, shown by large φ_R in EIG_0 and Kelvin waves.

4 Discussion

4.1 Which produces a more realistic feedback, GPCPv1.3 or v3.2?

Although GPCPv3.2 shows great improvements in precipitation estimates relative to in-situ observations (Li et al., 2023), whether it yields more accurate estimates of the greenhouse enhancement factor is less apparent. TRMM products that are used in producing GPCPv3.2 precipitation have positive 1-13% biases for monthly precipitation in the Indo-Pacific warm pool compared to in-situ atoll sites (Bolvin et al., 2021; Prakash et al., 2013). IMERG version 06B in general overestimates overall rainfall while underestimating very light rainfall (< 0.5 mm day^{-1}) (Prakash & Gairola, 2014). The above biases imply an underestimated greenhouse enhancement factor. Reconstructing Figures 3a-b using data from the Dynamics of the Madden-Julian Oscillation (DYNAMO) field campaign period (11 October 2011 to 8 February 2012) for the region [3°S-1°N; 71°E-75°E] yields feedbacks parameter of 0.17 in GPCPv1.3 and 0.12 in GPCPv3.2, which is smaller than 0.2 based on ground-based radar observations near Gan Island in Ciesielski et al. (2017). While GPCPv1.3 underestimates the spread in intensity of rainfall (Li et al., 2023), the above literature and evidence collectively suggests that GPCPv3.2 may overestimate tropical oceanic precipitation intensity and underestimate the greenhouse enhancement factor. The actual greenhouse enhancement factor may fall between values estimated using GPCPv3.2 and GPCPv1.3, and probably closer to the estimation by GPCPv3.2 given the much better match of rainfall intensity in GPCPv3.2 compared to in-situ observations (Li et al., 2023).

4.2 The large φ_R in EIG_0 and Kelvin waves obtained by GPCPv3.2

A robust phase shift between OLR and precipitation, or φ_R, is found in high-frequency eastward-propagating Kelvin waves and EIG_0 that is much larger when using GPCPv3.2 (Figure 4h) compared to using GPCPv1.3 (Figure 4g). The improved temporal frequency of precipitation observations in GPCPv3.2 suggests that this observed lag of the radiative feedback is real, but was not as apparent in previous datasets possibly due to lower sampling rates of precipitation observations. Despite the robustness, the magnitudes of the φ_R are mildly sensitive to the selection of OLR products (Figure S3 in the Supplemental Material).

It is unclear why the phase shift only appears in fast eastward-propagating waves. Some studies have found vertically-tilted structures in Kelvin waves and other gravity-modulated waves (Inoue et al., 2020; Kiladis et al., 2009; Mapes et al., 2006; Yasunaga & Mapes, 2012), but how the implied time lag in radiative heating contributes to the development of the waves is rarely discussed. The existence of large φ_R in Kelvin waves and EIG_0 and small φ_R in the MJO conflicts the result from Najarian and Sakaeda (2023), who suggest a 45° and 0° phase difference between cloud radiative heating and precipitation in the MJO and Kelvin waves, respectively. Lags of radiative heating of around 5 days behind precipitation as shown in Ciesielski et al. (2017) and Del Genio and Chen (2015) suggest an φ_R of ∼30° (assuming a 60-day MJO period), larger than our calcu-

lated φ_R of $\sim$15° in the MJO band (Figure 4h). We hypothesize that these inconsistencies may originate from the spatial and temporal ranges of the datasets used, and the precise way the MJO and Kelvin waves are defined.

5 Summary

Longwave cloud-radiative feedbacks have been hypothesized to be important for supporting tropical disturbances. This study examines the greenhouse enhancement factor measured as the ratio between negative OLR anomalies and surface precipitation, using two versions of the daily GPCP precipitation product versus NOAA OLR. GPCPv3.2 has less frequent precipitation between 10-40 mm day^{-1}, but more frequent precipitation at weaker and stronger intensities than in GPCPv1.3 (Figure 1). Calculating the climatological greenhouse enhancement factor using annual-mean climatological OLR and precipitation (Figure 2), GPCPv3.2 (0.18) yields a slightly smaller value than using GPCPv1.3 (0.20).

The radiative feedback is also assessed in the MJO band using 20-100 day filtered precipitation and OLR over the Indo-Pacific warm pool (Figure 3). When not considering spatial scale, GPCPv3.2 yields a much smaller greenhouse enhancement factor (0.09) than using GPCPv1.3 (0.15). The zonal scale-dependence of the greenhouse enhancement factor is qualitatively similar using either GPCP product, in that the feedback decreases as zonal planetary wavenumber increases, consistent with its role in setting the scale selection of the MJO in moisture mode theories (Adames & Kim, 2016). Relative to the magnitudes at low zonal wavenumbers, the factor is more strongly damped at higher wavenumbers in GPCPv3.2 compared to GPCPv1.3, suggesting a stronger scale selection in GPCPv3.2.

In $k-\omega$ spectral space, the radiative feedback parameter (r) resembles a red noise-like distribution using either precipitation product, in that the radiative feedback is generally stronger at lower frequencies and zonal wavenumbers (Figures 4d-f). Since GPCPv3.2 has larger variance than GPCPv1.3 precipitation (Figures 4a-c), an overall weaker r is shown (Figures 4d-f), consistent with the results above using broader spectral domains. Interestingly, the phase shift between OLR and precipitation, φ_R, is as large as 40° in certain fast eastward-propagating waves (Kelvin waves and n = 0 inertia-gravity wave) when calculated by GPCPv3.2, a feature much less robust using GPCPv1.3. The reason for this asymmetry in φ_R between fast eastward- and westward-propagating waves is unclear.

Longwave cloud-radiative feedbacks have been hypothesized to explain the scale selection and the growth of the MJO in moisture mode theory (Adames & Kim, 2016; A. Sobel & Maloney, 2012). Our result suggests that radiative heating provides a stronger scale selection mechanism for the MJO than previously considered, although how much moistening is supported by radiative heating at lower wavenumbers may be quantitatively overestimated in past results. If the greenhouse enhancement factor is smaller than past observation estimates, other supporting feedbacks such as surface latent heat flux and frictional convergence (e.g., Hu & Randall, 1994; Maloney & Sobel, 2004; A. H. Sobel et al., 2008, 2010; A. Sobel & Maloney, 2013; de Szoeke & Maloney, 2020) may be more important in destabilizing the MJO and possibly other tropical systems than previously thought.

Open Research

Data used in this manuscript can be accessed online (GPCPv1.3: `https://www.ncei.noaa.gov/access/metadata/landing-page/bin/iso?id=gov.noaa.ncdc:C00999`; GPCPv3.2: `https://disc.gsfc.nasa.gov/datasets/GPCPDAY_3.2/summary`; NOAA OLR: `https://psl.noaa.gov/data/gridded/data.olrcdr.interp.html`; NOAA NCEI OLR CDR daily:

https://www.ncei.noaa.gov/products/climate-data-records/outgoing-longwave-radiation-daily; CERES SYN1deg: https://ceres.larc.nasa.gov/data/). Available data DOI is provided (GPCPv1.3: 10.7289/V5RX998Z; GPCPv3.2: 10.5067/MEASURES/GPCP/DATA305; NOAA NCEI OLR CDR daily: 10.7289/V5SJ1HH2). Figures in this manuscript are made by ProPlot.

Acknowledgments

This material is based upon work supported by the National Aeronautics and Space Administration under Grant No. 80NSSC20K1105 issued through the NASA Energy and Water Cycle Study (NEWS), NSF grant AGS-2217785, and NOAA CVP grant NA22OAR4310609. W.-T. Hsiao is also supported by the Taiwan Ministry of Education Government Scholarship to Study Abroad (GSSA). The manuscript is aided by the discussion with Christian Kummerow, Nicolas Leitmann-Niimi, and Paul Stackhouse. We thank Ángel Adames-Corraliza for sharing insights on the zonal filtering for generating Figure 3.

References

Adames, Á. F., & Kim, D. (2016, March). The MJO as a dispersive, convectively coupled moisture wave: Theory and observations. *J. Atmos. Sci.*, *73*(3), 913–941.

Andersen, J. A., & Kuang, Z. (2012, April). Moist static energy budget of MJO-like disturbances in the atmosphere of a zonally symmetric aquaplanet. *J. Clim.*, *25*(8), 2782–2804.

Benedict, J. J., Medeiros, B., Clement, A. C., & Olson, J. G. (2020, May). Investigating the role of cloud-radiation interactions in subseasonal tropical disturbances. *Geophys. Res. Lett.*, *47*(9), e2019GL086817.

Bolvin, D. T., Huffman, G. J., Nelkin, E. J., & Tan, J. (2021, July). Comparison of monthly IMERG precipitation estimates with PACRAIN atoll observations. *J. Hydrometeorol.*, *22*(7), 1745–1753.

Bretherton, C. S., & Sobel, A. H. (2002, October). A simple model of a convectively coupled walker circulation using the weak temperature gradient approximation. *J. Clim.*, *15*(20), 2907–2920.

Bretherton, C. S., Widmann, M., Dymnikov, V. P., Wallace, J. M., & Bladé, I. (1999, July). The effective number of spatial degrees of freedom of a Time-Varying field. *J. Clim.*, *12*(7), 1990–2009.

Chikira, M. (2014, February). Eastward-Propagating intraseasonal oscillation represented by Chikira–Sugiyama cumulus parameterization. part II: Understanding moisture variation under weak temperature gradient balance. *J. Atmos. Sci.*, *71*(2), 615–639.

Ciesielski, P. E., Johnson, R. H., Jiang, X., Zhang, Y., & Xie, S. (2017, March). Relationships between radiation, clouds, and convection during DYNAMO. *J. Geophys. Res. D: Atmos.*, *122*(5), 2529–2548.

Crueger, T., & Stevens, B. (2015, June). The effect of atmospheric radiative heating by clouds on the Madden-Julian oscillation. *J. Adv. Model. Earth Syst.*, *7*(2), 854–864.

Del Genio, A. D., & Chen, Y. (2015, June). Cloud-radiative driving of the Madden-Julian oscillation as seen by the A-Train. *J. Geophys. Res. D: Atmos.*, *120*(11), 5344–5356.

de Szoeke, S. P., & Maloney, E. D. (2020, January). Atmospheric mixed layer convergence from observed MJO sea surface temperature anomalies. *J. Clim.*, *33*(2), 547–558.

Dias, J., Tulich, S. N., Gehne, M., & Kiladis, G. N. (2021, June). Tropical origins of weeks 2-4 forecasts errors during northern hemisphere cool season. *Mon. Weather Rev.*, *-1*(aop).

Doelling, D. R., Sun, M., Nguyen, L. T., Nordeen, M. L., Haney, C. O., Keyes, D. F., & Mlynczak, P. E. (2016, March). Advances in Geostationary-Derived longwave fluxes for the CERES synoptic (SYN1deg) product. *J. Atmos. Ocean. Technol.*, *33*(3), 503–521.

Ferrett, S., Yang, G.-Y., Woolnough, S. J., Methven, J., Hodges, K., & Holloway, C. E. (2020, January). Linking extreme precipitation in southeast asia to equatorial waves. *Quart. J. Roy. Meteor. Soc.*, *146*(727), 665–684.

Frank, W. M., & Roundy, P. E. (2006, September). The role of tropical waves in tropical cyclogenesis. *Mon. Weather Rev.*, *134*(9), 2397–2417.

Hayashi, Y. (1971). A generalized method of resolving disturbances into progressive and retrogressive waves by space fourier and time Cross-Spectral analyses. *Journal of the Meteorological Society of Japan. Ser. II*, *49*(2), 125–128.

Hou, A. Y., Kakar, R. K., Neeck, S., Azarbarzin, A. A., Kummerow, C. D., Kojima, M., ... Iguchi, T. (2014, May). The global precipitation measurement mission. *Bull. Am. Meteorol. Soc.*, *95*(5), 701–722.

Hsiao, W.-T., Barnes, E. A., Maloney, E. D., Tulich, S. N., Dias, J., & Kiladis, G. N. (2022, March). Role of the tropics in state-dependent improvements of US west coast NOAA unified forecast system precipitation forecasts. *Geophys. Res. Lett.*, *49*(5).

Hsiao, W.-T., Hwang, Y.-T., Chen, Y.-J., & Kang, S. M. (2022, June). The role of clouds in shaping tropical pacific response pattern to extratropical thermal forcing. *Geophys. Res. Lett.*, *49*(11).

Hu, Q., & Randall, D. A. (1994, April). Low-Frequency oscillations in Radiative-Convective systems. *J. Atmos. Sci.*, *51*(8), 1089–1099.

Huffman, G. J., Adler, R. F., Behrangi, A., Bolvin, D. T., Nelkin, E. J., & Ehsani, M. R. (2023). Algorithm theoretical basis document (ATBD) for global precipitation climatology project version 3.2 precipitation data [Computer software manual].

Huffman, G. J., Adler, R. F., Morrissey, M. M., Bolvin, D. T., Curtis, S., Joyce, R., ... Susskind, J. (2001, February). Global precipitation at One-Degree daily resolution from multisatellite observations. *J. Hydrometeorol.*, *2*(1), 36–50.

Inoue, K., Adames, Á. F., & Yasunaga, K. (2020, May). Vertical velocity profiles in convectively coupled equatorial waves and MJO: New diagnoses of vertical velocity profiles in the Wavenumber–Frequency domain. *J. Atmos. Sci.*, *77*(6), 2139–2162.

Jiang, X., Adames, Á. F., Kim, D., Maloney, E. D., Lin, H., Kim, H., ... Klingaman, N. P. (2020, September). Fifty years of research on the madden-julian oscillation: Recent progress, challenges, and perspectives. *J. Geophys. Res.*, *125*(17), e2019JD030911.

Johnson, R. H., & Ciesielski, P. E. (2000, May). Rainfall and radiative heating rates from TOGA COARE atmospheric budgets. *J. Atmos. Sci.*, *57*(10), 1497–1514.

Johnson, R. H., Ciesielski, P. E., Ruppert, J. H., & Katsumata, M. (2015, February). Sounding-Based thermodynamic budgets for DYNAMO. *J. Atmos. Sci.*, *72*(2), 598–622.

Kiladis, G. N., Wheeler, M. C., Haertel, P. T., Straub, K. H., & Roundy, P. E. (2009, April). Convectively coupled equatorial waves. *Rev. Geophys.*, *47*(2).

Kim, D., Ahn, M.-S., Kang, I.-S., & Del Genio, A. D. (2015, September). Role of longwave Cloud–Radiation feedback in the simulation of the Madden–Julian oscillation. *J. Clim.*, *28*(17), 6979–6994.

Kummerow, C., Barnes, W., Kozu, T., Shiue, J., & Simpson, J. (1998, June). The tropical rainfall measuring mission (TRMM) sensor package. *J. Atmos. Ocean. Technol.*, *15*(3), 809–817.

Lee, H.-T., Gruber, A., Ellingson, R. G., & Laszlo, I. (2007, December). Development of the HIRS outgoing longwave radiation climate dataset. *J. Atmos.*

Ocean. Technol., *24*(12), 2029–2047.

Lee, M.-I., Kang, I.-S., Kim, J.-K., & Mapes, B. E. (2001, July). Influence of cloud-radiation interaction on simulating tropical intraseasonal oscillation with an atmospheric general circulation model. *J. Geophys. Res.*, *106*(D13), 14219–14233.

Li, Z., Thompson, E. J., Behrangi, A., Chen, H., & Yang, J. (2023, June). Performance of GPCP daily products over oceans: Evaluation using passive aquatic listeners. *Geophys. Res. Lett.*, *50*(11), e2023GL104310.

Liebmann, B., & Smith, C. A. (1996). Description of a complete (interpolated) outgoing longwave radiation dataset. *Bull. Am. Meteorol. Soc.*, *77*(6), 1275–1277.

Lin, J.-L., & Mapes, B. E. (2004, August). Radiation budget of the tropical intraseasonal oscillation. *J. Atmos. Sci.*, *61*(16), 2050–2062.

Ma, D., & Kuang, Z. (2011, November). Modulation of radiative heating by the Madden-Julian oscillation and convectively coupled kelvin waves as observed by CloudSat. *Geophys. Res. Lett.*, *38*(21).

Maloney, E. D., & Hartmann, D. L. (2000, May). Modulation of eastern north pacific hurricanes by the Madden–Julian oscillation. *J. Clim.*, *13*(9), 1451–1460.

Maloney, E. D., & Sobel, A. H. (2004, November). Surface fluxes and ocean coupling in the tropical intraseasonal oscillation. *J. Clim.*, *17*(22), 4368–4386.

Mapes, B., Tulich, S., Lin, J., & Zuidema, P. (2006, December). The mesoscale convection life cycle: Building block or prototype for large-scale tropical waves? *Dyn. Atmos. Oceans*, *42*(1), 3–29.

Medeiros, B., Clement, A. C., Benedict, J. J., & Zhang, B. (2021, March). Investigating the impact of cloud-radiative feedbacks on tropical precipitation extremes. *npj Climate and Atmospheric Science*, *4*(1), 1–10.

Najarian, H., & Sakaeda, N. (2023, April). The influence of cloud types on cloud-radiative forcing during DYNAMO/AMIE. *J. Geophys. Res.*, *128*(8).

Peters, M. E., & Bretherton, C. S. (2005, October). A simplified model of the walker circulation with an interactive ocean mixed layer and Cloud-Radiative feedbacks. *J. Clim.*, *18*(20), 4216–4234.

Prakash, S., & Gairola, R. M. (2014, February). Validation of TRMM-3B42 precipitation product over the tropical indian ocean using rain gauge data from the RAMA buoy array. *Theor. Appl. Climatol.*, *115*(3), 451–460.

Prakash, S., Mahesh, C., & Gairola, R. M. (2013, July). Comparison of TRMM multi-satellite precipitation analysis (TMPA)-3B43 version 6 and 7 products with rain gauge data from ocean buoys. *Remote Sens. Lett.*, *4*(7), 677–685.

Prigent, C. (2010, April). Precipitation retrieval from space: An overview. *C. R. Geosci.*, *342*(4), 380–389.

Raymond, D. J. (2001, September). A new model of the Madden–Julian oscillation. *J. Atmos. Sci.*, *58*(18), 2807–2819.

Raymond, D. J., Sessions, S. L., Sobel, A. H., & Fuchs, Ž. (2009, March). The mechanics of gross moist stability. *J. Adv. Model. Earth Syst.*, *1*(3).

Ruppert, J. H., Wing, A. A., Tang, X., & Duran, E. L. (2020). The critical role of cloud–infrared radiation feedback in tropical cyclone development. *Proceedings of the National Academy of Sciences*, *117*(45), 27884–27892.

Sobel, A., & Maloney, E. (2012, May). An idealized Semi-Empirical framework for modeling the Madden–Julian oscillation. *J. Atmos. Sci.*, *69*(5), 1691–1705.

Sobel, A., & Maloney, E. (2013, January). Moisture modes and the eastward propagation of the MJO. *J. Atmos. Sci.*, *70*(1), 187–192.

Sobel, A., Wang, S., & Kim, D. (2014, November). Moist static energy budget of the MJO during DYNAMO. *J. Atmos. Sci.*, *71*(11), 4276–4291.

Sobel, A. H., & Gildor, H. (2003, December). A simple Time-Dependent model of SST hot spots. *J. Clim.*, *16*(23), 3978–3992.

Sobel, A. H., Maloney, E. D., Bellon, G., & Frierson, D. M. (2008, September). The role of surface heat fluxes in tropical intraseasonal oscillations. *Nat. Geosci.*,

1(10), 653–657.

Sobel, A. H., Maloney, E. D., Bellon, G., & Frierson, D. M. (2010, January). Surface fluxes and tropical intraseasonal variability: a reassessment. *Journal of Advances in Modeling Earth Systems*, *2*(1).

Su, H., & David Neelin, J. (2002, September). Teleconnection mechanisms for tropical pacific descent anomalies during el niño. *J. Atmos. Sci.*, *59*(18), 2694–2712.

Sugiyama, M. (2009, June). The moisture mode in the Quasi-Equilibrium tropical circulation model. part i: Analysis based on the weak temperature gradient approximation. *J. Atmos. Sci.*, *66*(6), 1507–1523.

Takayabu, Y. N. (1994). Large-Scale cloud disturbances associated with equatorial waves. *Journal of the Meteorological Society of Japan. Ser. II*, *72*(3), 433–449.

Tseng, K.-C., Barnes, E. A., & Maloney, E. D. (2018, January). Prediction of the midlatitude response to strong Madden-Julian oscillation events on S2S time scales. *Geophys. Res. Lett.*, *45*(1), 463–470.

Wheeler, M., & Kiladis, G. N. (1999, February). Convectively coupled equatorial waves: Analysis of clouds and temperature in the Wavenumber–Frequency domain. *J. Atmos. Sci.*, *56*(3), 374–399.

Wolding, B. O., & Maloney, E. D. (2015, October). Objective diagnostics and the Madden–Julian oscillation. part II: Application to moist static energy and moisture budgets. *J. Clim.*, *28*(19), 7786–7808.

Yasunaga, K., & Mapes, B. (2012, January). Differences between more divergent and more rotational types of convectively coupled equatorial waves. part i: Space–Time spectral analyses. *J. Atmos. Sci.*, *69*(1), 3–16.

Zhang, C., Adames, Á. F., Khouider, B., Wang, B., & Yang, D. (2020, September). Four theories of the Madden-Julian oscillation. *Rev. Geophys.*, *58*(3), e2019RG000685.

Zurovac-Jevtić, D., Bony, S., & Emanuel, K. (2006, August). On the role of clouds and moisture in tropical waves: A Two-Dimensional model study. *J. Atmos. Sci.*, *63*(8), 2140–2155.

Figure 1.

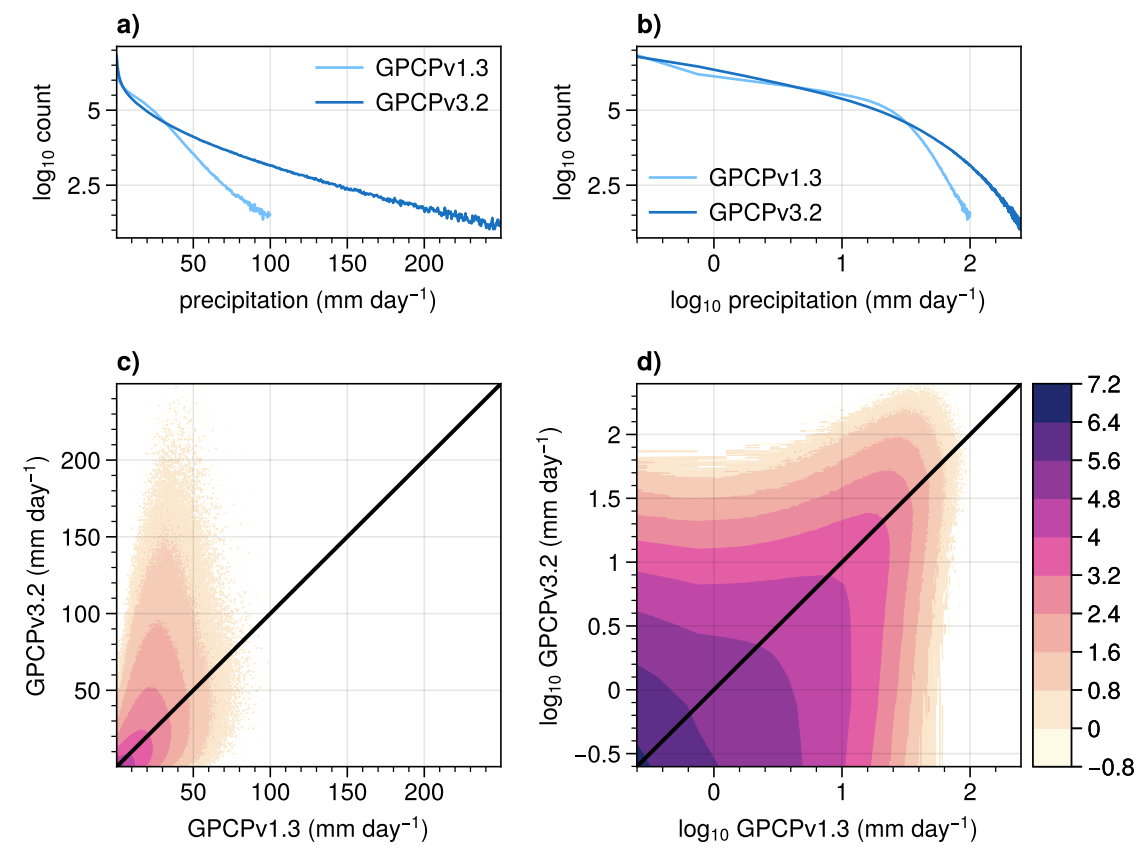
a)
GPCPv1.3
GPCPv3.2
log10 count
5
2.5
50
100
150
200
precipitation (mm day−1)
b)
GPCPv1.3
GPCPv3.2
log10 count
5
2.5
0
1
2
log10 precipitation (mm day−1)
c)
GPCPv3.2 (mm day−1)
200
150
100
50
50
100
150
200
GPCPv1.3 (mm day−1)
d)
log10 GPCPv3.2 (mm day−1)
2
1.5
1
0.5
0
−0.5
0
1
2
log10 GPCPv1.3 (mm day−1)
7.2
6.4
5.6
4.8
4
3.2
2.4
1.6
0.8
0
−0.8

Figure 2.

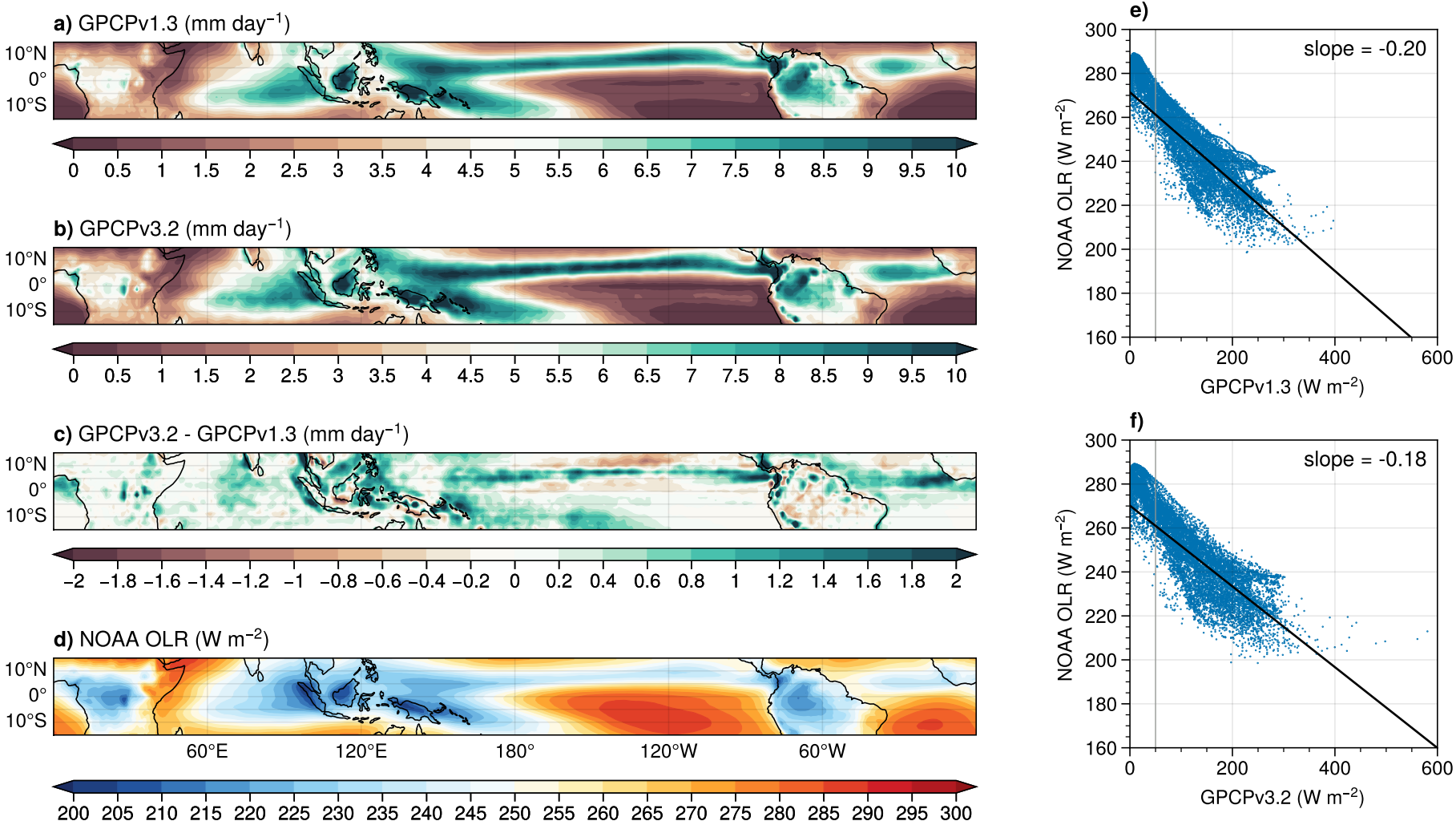
a) GPCPv1.3 (mm day−1)
10°N
0°
10°S
0 0.5 1 1.5 2 2.5 3 3.5 4 4.5 5 5.5 6 6.5 7 7.5 8 8.5 9 9.5 10
b) GPCPv3.2 (mm day−1)
10°N
0°
10°S
0 0.5 1 1.5 2 2.5 3 3.5 4 4.5 5 5.5 6 6.5 7 7.5 8 8.5 9 9.5 10
c) GPCPv3.2 - GPCPv1.3 (mm day−1)
10°N
0°
10°S
−2 −1.8 −1.6 −1.4 −1.2 −1 −0.8 −0.6 −0.4 −0.2 0 0.2 0.4 0.6 0.8 1 1.2 1.4 1.6 1.8 2
d) NOAA OLR (W m−2)
10°N
0°
10°S
60°E 120°E 180° 120°W 60°W
200 205 210 215 220 225 230 235 240 245 250 255 260 265 270 275 280 285 290 295 300
e)
slope = -0.20
NOAA OLR (W m−2)
GPCPv1.3 (W m−2)
300 280 260 240 220 200 180 160
0 200 400 600
f)
slope = -0.18
NOAA OLR (W m−2)
GPCPv3.2 (W m−2)
300 280 260 240 220 200 180 160
0 200 400 600

Figure 3.

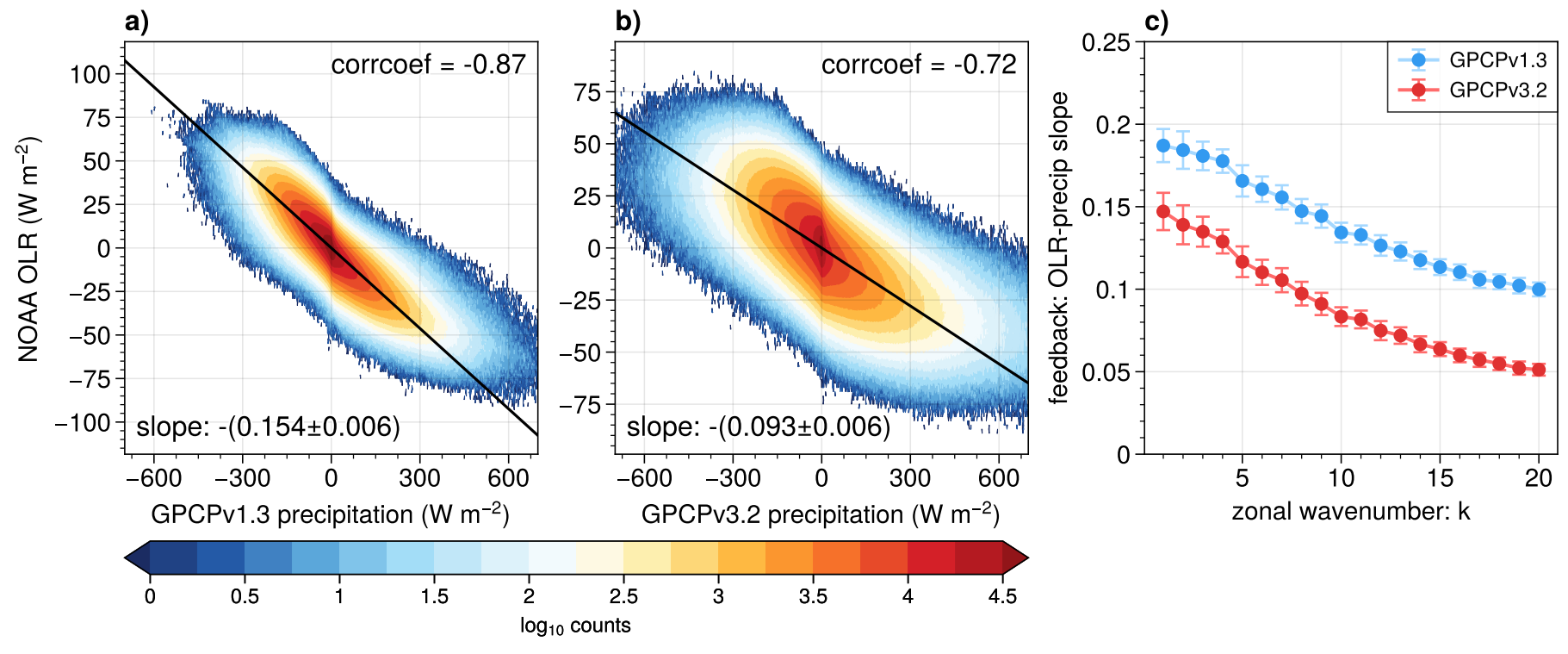
a)
corrcoef = -0.87
slope: -(0.154±0.006)
NOAA OLR (W m^{-2})
GPCPv1.3 precipitation (W m^{-2})
b)
corrcoef = -0.72
slope: -(0.093±0.006)
GPCPv3.2 precipitation (W m^{-2})
log$_{10}$ counts
c)
GPCPv1.3
GPCPv3.2
feedback: OLR-precip slope
zonal wavenumber: k

Figure 4.

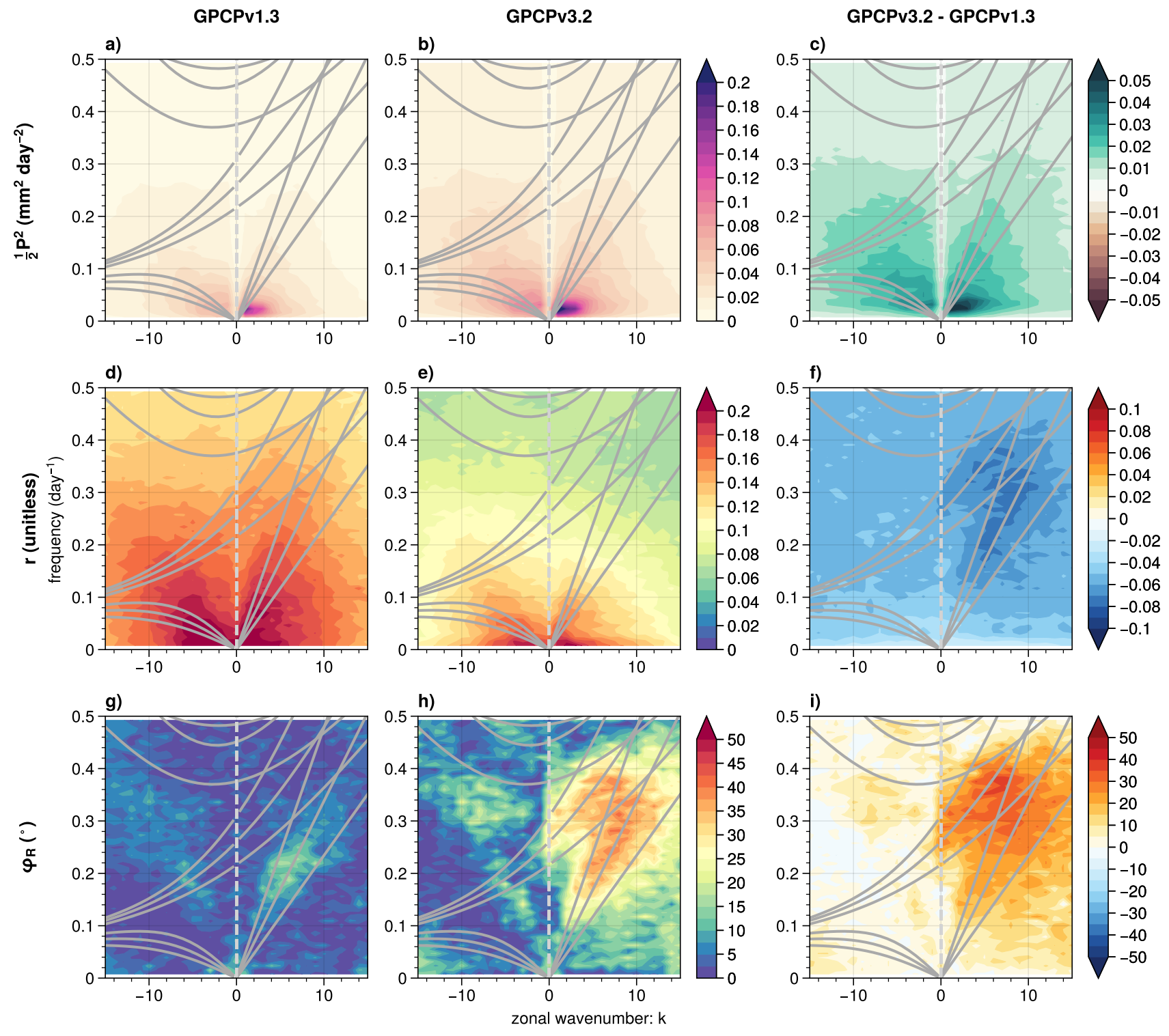
GPCPv1.3
GPCPv3.2
GPCPv3.2 - GPCPv1.3
a)
b)
c)
d)
e)
f)
g)
h)
i)
½P² (mm² day⁻²)
r (unitless)
frequency (day⁻¹)
φR (°)
zonal wavenumber: k